Robotics and Autonomous Systems 154 (2022) 104134

Contents lists available at ScienceDirect

Robotics and Autonomous Systems

journal homepage: www.elsevier.com/locate/robot

Multimodality robotic systems: Integrated combined legged-aerial mobility for subterranean search-and-rescue

Björn Lindqvist [a,*], Samuel Karlsson [a], Anton Koval [a], Ilias Tevetzidis [a], Jakub Haluška [a], Christoforos Kanellakis [a], Ali-akbar Agha-mohammadi [b], George Nikolakopoulos [a]

[a] Robotics and AI Team, Department of Computer, Electrical and Space Engineering, Luleå University of Technology, Laboratorievägen 14, 971 87 Luleä, Sweden

[b] Jet Propulsion Laboratory California Institute of Technology Pasadena, CA, 91109, United States of America

ARTICLE INFO

Article history:
Received 17 November 2021
Received in revised form 21 March 2022
Accepted 20 April 2022
Available online 6 May 2022

Keywords:
Field robotics
Search-and-rescue robotics
Unmanned aerial vehicles
Quadruped robots
Multimodality robots
Subterranean exploration

ABSTRACT

This work presents a field-hardened autonomous multimodal legged-aerial robotic system for subterranean exploration, extending a legged robot to be the carrier of an aerial platform capable of a rapid deployment in search-and-rescue scenarios. The driving force for developing such robotic configurations are the requirements for large-scale and long-term missions, where the payload capacity and long battery life of the legged robot is combined and integrated with the agile motion of the aerial agent. The multimodal robot is structured around the quadruped Boston Dynamics Spot, enhanced with a custom configured autonomy sensor payload as well as a UAV carrier platform, while the aerial agent is a custom built quadcopter. This work presents the novel design and hardware implementation as well as the onboard sensor suites. Moreover it establishes the overall autonomy architecture in a unified supervision approach while respecting each locomotion modality, including guidance, navigation, perception, state estimation, and control capabilities with a focus on rapid deployment and efficient exploration. The robotic system complete architecture is evaluated in real subterranean tunnel areas, in multiple fully autonomous search-and-rescue missions with the goal of identifying and locating objects of interest within the subterranean environment.

1. Introduction and background

The area of autonomous subterranean search-and-rescue has grown significantly in the last years due to the fact that it was the focus and primary selected application area of the DARPA Robotics Challenge [1]. In this case, teams of robots are tasked with exploring vast subterranean areas (tunnels, urban areas, caves) for identifying and locating specific hidden objects of interest such as survivors, tools, gas leaks, etc. The application areas of this new technology ranges from mapping and inspecting caves [2,3], inspection and safety in the mining industry [4,5], monitoring for natural disasters [6] or even in the search for extraterrestrial life in subterranean systems on other planets or asteroids [7,8]. Terrain in SubT environments commonly has uneven structures which expands both horizontally and vertically. Seismic events, or man-made excavation, can do severe damage to such types of environments as depicted in Fig. 1. Moreover, it may block human workers from exiting dangerous areas, and makes it dangerous for human teams to carry out rescue operations. This creates a necessity of deploying robots in such scenarios. However, every robotic platform has its own advantages and disadvantages which makes it hard to design a single capable platform, as was demonstrated during the SubT Challenge where teams were using wheeled, legged, and aerial robots. There have been greatly successful efforts in the deployment of both aerial robots [9,10], as well as ground or legged robots [9,11,12], but both approaches have limiting factors: ground robots cannot move over rough terrain, such as after rockfalls, nor complete the mission if passages are blocked or there is some other sudden vertical displacement of the terrain, as depicted in Fig. 1. In contrary to ground robots, aerial robots have limited battery endurance when equipped with extra payload that incorporates a full sensor suite with onboard computation power. This payload is required to allow them to execute a fully autonomous exploration or search-and-rescue task and limits their maximum mission duration e.g. there is a sharp trade-off between autonomy level and flight time [11]. However, for aerial robots the traversability level of ground terrain is irrelevant, and access to blocked passages is only limited by the size of the aerial robot. A summary of the advantages and disadvantages of aerial, legged and wheeled robotic platforms in SubT exploration and search-and-rescue missions is presented in Table 1.

* Corresponding author.
E-mail address: bjolin@ltu.se (B. Lindqvist).

https://doi.org/10.1016/j.robot.2022.104134

Fig. 1. Examples of rockfalls after seismic events in the underground mines [13].

Due to these kinds of challenges, hybrid locomotion and multimodal robots have shown promising results in a variety of tasks where extending the terrain traversability of the robot is critical, such as; wheeled-legged robots for inspection tasks in difficult terrain [14], air-actuated wheeled-climbing robots [15], or adding magnetic adhesion to mobile robots for traversing ferromagnetic inclined surfaces [16–18]. For combining ground and aerial capabilities, robots such as the Drivocopter [19] have been attempted as well. The main motivation for the combined or multimodal design of the robotic system is the increased searching area coverage with an efficient utilization of advantages of each robot modality.

Thus, this article presents a different novel direction, where a legged ground robot acts as the carrier of an aerial agent forming a multimodality combined robot system, thus mitigating the expended flight time to reach the desired exploration location (e.g. the blocked passage, or hard-to-reach area) without sacrificing mobility.

To summarize: as autonomy requirements, mission complexity, and the need for abilities in handling unforeseen terrain challenges increases, the proposed multimodality approach to hybrid locomotion will be on the forefront of critical mission applications in terrestrial subterranean search-and-rescue, but also in the search for life in subterranean caverns on other planets [20]. Solving these challenges is the primary justification behind the proposed research efforts into legged-aerial robot unification with the long-term goal of extending the mission capabilities of existing robotic solutions when entering completely unknown and unknowable environments and their related terrain traversability challenges.

Towards that goal, and as part of the NeBula autonomy framework [11,21,22] and the Team CoSTAR [23], this article aims to establish a baseline solution for allowing a combined fully autonomous field mission in realistic evaluation scenarios, performed in relevant subterranean tunnel environments.

2. Contributions

The main contributions to the state-of-the-art is as follows: (1) the design and construction of a novel fully integrated robotic system (hardware and software) capable of full autonomy, including sensor suites selected for mission execution in subterranean environments. (2) The combined software architecture that uses a legged-aerial system to execute a search-and-rescue (object detection and localization) mission, and the related mission design. (3) A realistic field evaluation of the autonomy capabilities of the proposed multimodality system, in relevant subterranean GPS- and communication-denied environments. These contributions establish a baseline for future developments and acts as an enabler for the multimodality technology, and with the included field evaluations offers a significant contribution towards the general area of multimodality robots for search-and-rescue robotics in subterranean environments. Finally, it should be highlighted that we are presenting this work as the complete system, and not on the level of individual sub-components.

3. Outline

The rest of the work is structured as follows: First, the robots designed specifically for the SubT mission are introduced in Section 4. Next in Section 5 an overall high-level description of the autonomy kits, used for the combined robot system is presented including navigation, estimation, object detection, and the combined mission behavior. In Section 6 the experiment set-up and operator interactions are considered, as well as a presentation of the experimental validation results and associated experiment video. Lastly, directions for future work are offered in Section 7 and the article is concluded in Section 8.

4. Robot design

4.1. UAV robot

The utilized Unmanned Aerial Vehicle (UAV) is custom built at the Robotics and AI Team at Luleå University of Technology. The aerial vehicle is specifically designed for subterranean missions, built to be as compact as possible (to allow for a flight through constrained environments), while still being able to carry a sensor suite and computation payload that allows for the autonomous subterranean mission. The aerial vehicle can be seen in its carried position in Fig. 2 (note: the UAV is here carried with its front facing the rear of the legged robot). The UAV is based around a 12-inch propeller design, while its dimensions are w $\times$ l $\times$ h 513 $\times$ 335 $\times$ 339 mm and the total weight is 3615 g. The UAV is equipped with a ski-style landing gear, designed to work with the UAV carrier platform mounted on the legged robot (Spot). The onboard computation is done by an Intel NUC 10 BXNUC10I5FNKPA2, as well as an Intel Neural Compute Stick 2. The onboard sensor suite is as follows: a forward-facing RealSense D455 RGB-D Camera, a downward-facing single-beam LiDAR Garmin LiDAR Lite v3, a top-mounted 360° Velodyne Puck Lite 3d LiDAR, and the Pixhawk Cube used for attitude control and for its internal IMU. Additionally, the UAV carries three LED stripes illuminating the areas in front and below. The UAV sensor suite is displayed in Fig. 3.

4.2. Spot sensor suite

In addition to the out-of-the-box sensors and computers on the Boston Dynamics Spot, we have added our own sensor and computation kit on top. The Spot kit also uses an Intel NUC 10 BXNUC10I5FNKPA2 for computation, and on top of the shoulders it carries a compact sensor assembly. This assembly consists of: 360° Velodyne Puck Lite 3d LiDAR, three RealSense D455

Table 1
Advantages and disadvantages of robotic platforms for missions in SubT environments.

Robot type	Pros	Cons
Aerial	• 3D Omnidirectional Movement • Fly to hard-to-reach areas • Quick and agile maneuvering • Ignores ground terrain challenges	• Short flight time (∼10–20 min but very design dependent) • Max payload: up to 30% of a platform weight • Wind gusts (ex. in mine shafts) can affect the flight stability
Legged	• Long run time (∼60 min) • Payload: up to 50% of the platform weight • Can handle uneven ground terrain. • 2D Omnidirectional Movement • No impact from wind disturbances	• Absence of motion in z direction • Cannot handle vertical terrain
Wheeled	• Long run time (∼180 min) • Payload: up to 150% of the platform weight • No impact from wind disturbances	• Absence of motion in z direction • Can only traverse relatively even surfaces • Can have difficulties maneuvering in tight spaces • Cannot handle vertical terrain

mounted forward, left, and right. It also carries a VectorNav VN-100 IMU and just as its aerial counterpart, LED strips illuminating the field of view of the cameras. In addition to the sensor assembly, it also carries a rear-mounted RealSense D455, and corresponding LED strips. On top of the rear section, Spot carries all its supporting components (Arduinos, battery, USB hub, electronics) and the UAV carrier platform. The Spot sensor suite can be seen in Fig. 3.

4.3. UAV carrier platform

The UAV carrier platform is designed with a manufacturing based on a 3D printer in mind thus, all the components could be printed on customer-grade FDM 3D printers, such as Ultimaker UM2+/UM3 or Prusa MK3. The core components are two V-rails, where the landing gear of the aerial agent is parked and locked in place, and the locking mechanism consists of a pair of clamps in each rail. These are controlled by the NEMA14 Stepper motor. Each of the clamps are secured in the locked state by a door-lock style solenoid and by default the clamps are closed and secured with the solenoids. This state does not require any power, and it provides a fail-safe in case of power shortage when the UAV is loaded. When the UAV is ready to take off, the unlocking sequence is performed: The door-lock style solenoids retract, the clamps can move freely and rotate to the open position and thus the UAV can now take off. This process is controlled using another onboard Arduino tied only to the carrier platform. The schematics of the landing platform can be found in Fig. 4.

5. System architecture

5.1. Mission definition

While this paper also focuses on the integration of aerial-legged mobility in general, evaluating the general architecture in a specific mission scenario provides a useful test-case for the autonomy capabilities. The test-case will be a simulated search-and-rescue mission in a subterranean environment comprised of narrow tunnel-like areas. A typical situation could be an accident in a mine or cave, where the whole area is dangerous to enter and the autonomous robots act as first responders to the scene in order to provide the 3D reconstruction and the locations of objects of interest in that area (for example survivors). The focus is on rapid deployment of the framework and the ability to reach the scene efficiently, not providing full exploration coverage of the area. The full mission of the legged-aerial explorer is as follows: from a known location of a passage or hard-to-reach area provided by the operator (assuming either previous knowledge of the area through a map or information provided by a previous run by another robot that detected the passage), the legged-aerial system should autonomously navigate to the deployment point p_{dep}, adjust itself for aerial-agent take-off and initialize the aerial autonomy. The aerial exploration mission is then launched and the aerial agent is tasked to survey the selected passage for a specified duration $T_{explore}$, while looking for the objects of interest. It should then return to the deployment point. During the aerial mission the legged robot is tasked to wait at a point p_{wait}. So in short: in this specific use case demonstration the quadruped robot acts as the UAV carrier to a pre-determined deployment point, while the UAV mission requires no previous knowledge of the area. As such, the autonomy capabilities described in Section 5.2.1 for the UAV, and in Section 5.2.2 for the legged robot, are specified for the completion of the mission this use case provides.

5.2. Guidance, navigation and control

The following Sections 5.2.1 and 5.2.2 will describe the components that constitute the complete autonomy architecture of the multimodality system. A high-level architecture of the robotic autonomy system can be found in Fig. 5. We denote aerial agent parameters with superscript a and Spot parameters with superscript s. Other parameters are described in the following sections.

5.2.1. UAV autonomy

The UAV autonomy is based around the currently-under-development COMPRA (COMpact and Reactive Autonomy) stack [24] developed specifically for autonomous subterranean tunnel missions. The framework is focused around rapid deployment, as well as resilient and low-complexity reactive autonomy solutions. COMPRA uses a state-of-the-art LiDAR-Inertial Odometry (LIO-SAM) [25] for 3D state estimation, using LiDAR pointcloud $\{P^a\}$ and IMU sensor data $\mathcal{I}^a$ as inputs, and produces the state vector as $X^a = [p_x, p_y, p_z, v_x, v_y, v_z, \phi, \theta, \psi, \omega_x, \omega_y, \omega_z]^\top$, e.g. position, velocity, angular, and angular velocity states. Let us also denote the UAV body-frame as the rotation of position and velocity states about the z-axis by yaw angle ψ as $X^{a,\mathcal{B}} = [p^{\mathcal{B}}, v^{\mathcal{B}}, \phi, \theta, \psi, \omega]^\top$. Additionally, the downward-facing single-beam LiDAR provides a local z-coordinate measurement (e.g. distance to the ground) as $p_z^{\mathbb{L}} = R_{sbl} \cos\theta \cos\phi$, where R_{sbl} is the range measurement.

Flight control is based on a cascaded structure using a non-linear model predictive controller (NMPC) [26,27] as the reference tracking controller and the Pixhawk Cube [28] for attitude control. The NMPC considers $x_{nmpc} = [p^{\mathcal{B}}, v^{\mathcal{B}}, \phi, \theta]$, and thus, operates in the UAV body frame. The generated control inputs are $u^a = [T, \theta_{ref}, \phi_{ref}]$ with $\phi_{\text{ref}} \in \mathbb{R}$, $\theta_{\text{ref}} \in \mathbb{R}$ and $T_{\text{ref}} \geq 0$ to be the references in roll, pitch and total mass-less thrust generated by the four rotors, which are very commonly accepted commands together with a yaw-rate command as $\dot{\psi}_{ref}$ as inputs to low level attitude controllers, with T_{ref} mapped to a control signal as u_t

Fig. 2. The legged-aerial explorer with its full sensor suite and the UAV carrier platform.

$\in [0, 1]$ to fit into the Pixhawk framework [29]. The yaw angle ψ is controlled with a decoupled simple PD controller.

To enable an autonomous navigation and exploration behavior, COMPRA applies two components: a reactive Artificial Potential Field (APF) formulation, based on instantaneous 3D LiDAR pointcloud data that maintains a safe distance from any objects or walls, and an effective heading regulation technique that uses depth-images from the onboard RGB-D camera to align the UAV body-frame with the deepest cluster of points, which we will denote as the Deepest-Point Heading Regulation (DPHR).

The 3D APF uses a repulsive force model similar to the classic APF proposed by Warren [30], while directly using the 3D LiDAR pointcloud by letting each point within a specified volume defined by radius r_F result in a repulsive force, and then summing all such point-forces to get the total. The benefit is that no in-between software that classifies obstacles, shapes, boundaries, etc. is required and as such the APF is independent on mappers or other such software, which is beneficial for a safety layer (as to not be affected by other systems performing incorrectly). Let us denote the local point cloud generated by the 3D LiDAR as $\{P^a\}$, where all points are described by a relative position to the LiDAR as $\rho = [\rho_x, \rho_y, \rho_z]$. Also denote the repulsive force as $F^r = [F_x^r, F_y^r, F_z^r]$. As we are only interested in points inside the radius of influence r_F when considering the repulsive force, let us

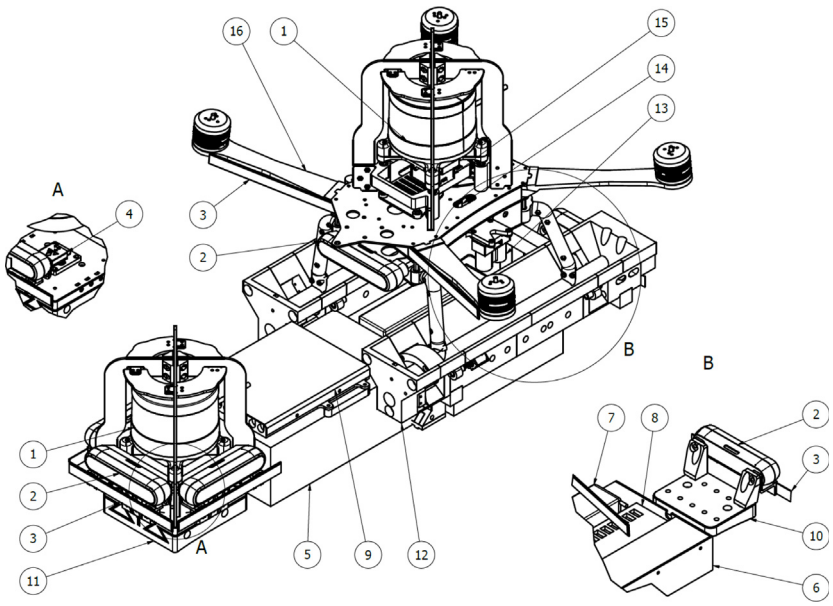

Fig. 3. Side view on the complete sensor suite. 1 — Velodyne PUCK lite, 2 — RealSense D455 camera, 3 — LED strip package, 4 — VectorNav VN-100 IMU, 5 — Intel NUC computer (Spot), 6 — Accessory box, 7 — Auxiliary LiPo battery, 8 — USB hub, 9 — cable organizer, 10 — Spot rear mounting plate, 11 — Spot front mounting plate, 12 — UAV carrier platform, 13 — Single beam LiDAR, 14 — Intel NUC computer (UAV), 15 — Pixhawk Flight controller, 16 — UAV.

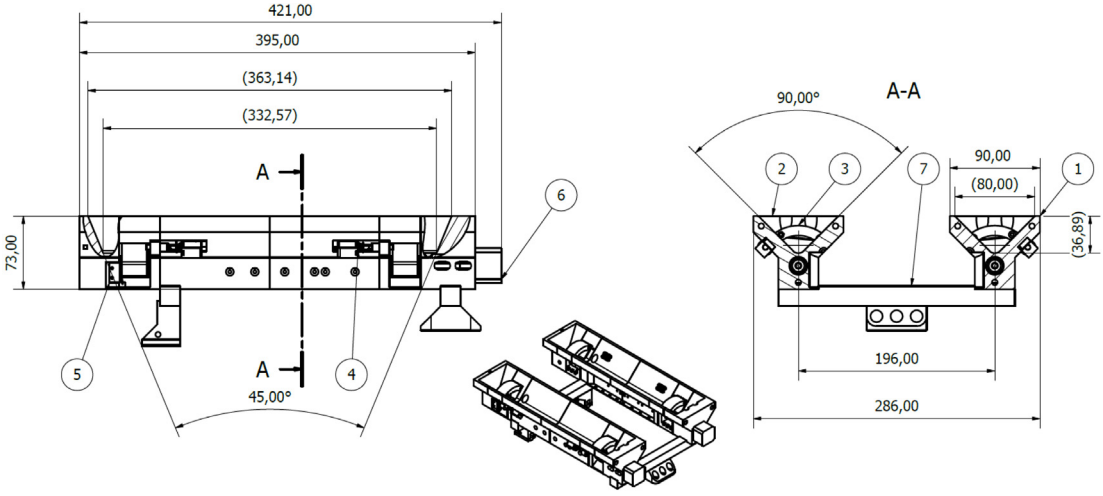

Fig. 4. The components of the UAV carrier platform. 1 — Left V-rail, 2 — Right V-rail, 3 — Locking clamp, 4 — Door-lock style solenoid, 5 — End stop, 6 -Stepper motor NEMA14, 7 — Spot mounting frame.

denote the list of such points $\boldsymbol{\rho}_r \in \{P\}$, where $|| \rho_r^i || \leq r_F$ and $i = 0, 1, \ldots, N_{\rho r}$ (and as such N_{ρ_r} is the number of points to be considered for the repulsive force). The repulsive force is:

$$F^r = \sum_{i=0}^{N_{\rho r}} L(1 - \frac{|| \rho_r^i ||}{r_F})^2 \frac{-\rho_r^i}{|| \rho_r^i ||} \tag{1}$$

where L is the repulsive constant and represents the largest possible force-per-point inside r_F. The attractive force F^{att} can be seen as the vector from $p^{\mathcal{B}}$ to the desired way-point as $F^{att} = wp^{a,\mathcal{B}} - \hat{p}^{\mathcal{B}}$. Additionally, we apply saturation limits on the force magnitude and the rate of change of the forces along each axis, as to enforce a more stable flight behavior so that rapid changes in the local pointcloud do not lead to jerky or oscillatory flight behavior of the UAV.

The DPHR uses the onboard RGB-D instantaneous camera stream to reactively find the deepest cluster of points within the stream. Initially, the recovered depth images from the sensor are filtered using a gray scale morphological close operation [31] as a preprocessing step to remove noise and enhance the tunnel opening. Afterwards, the clustering step is employed using a k-means methodology to extract a fixed number of clusters C_i, $[i = 1, 2, 3, \ldots, N_{clusters}]$, where the $N_{clusters} = 10$ value has been selected based on the tunnel environment morphology. Moreover, the mean intensity value for each cluster region is calculated and selects the cluster with the maximum intensity, which indicates the deepest parts of the tunnel. The x-axis pixel coordinate of the cluster centroid is calculated as $s_x = \frac{1}{|C_m|} \sum_{(x,y) \in C_m} x$, where $|C_m|$ represents the number of pixels. Finally, s_x is normalized and transformed with respect to the image principal point $\bar{s_x}$ and converted to a yaw rate reference $\dot{\psi}_{ref} \in [\min \max]$, using $\dot{\psi}_{ref} = \bar{s_x} * l$, where l maps linearly the yaw rate to min and max values. Therefore, the yaw angle ψ, which controls the UAV body x-axis direction is aligned with the tunnel direction based on the heading regulation technique.

During the exploration task, the UAV is tasked to maintain a specified distance to the ground, which is denoted by the local

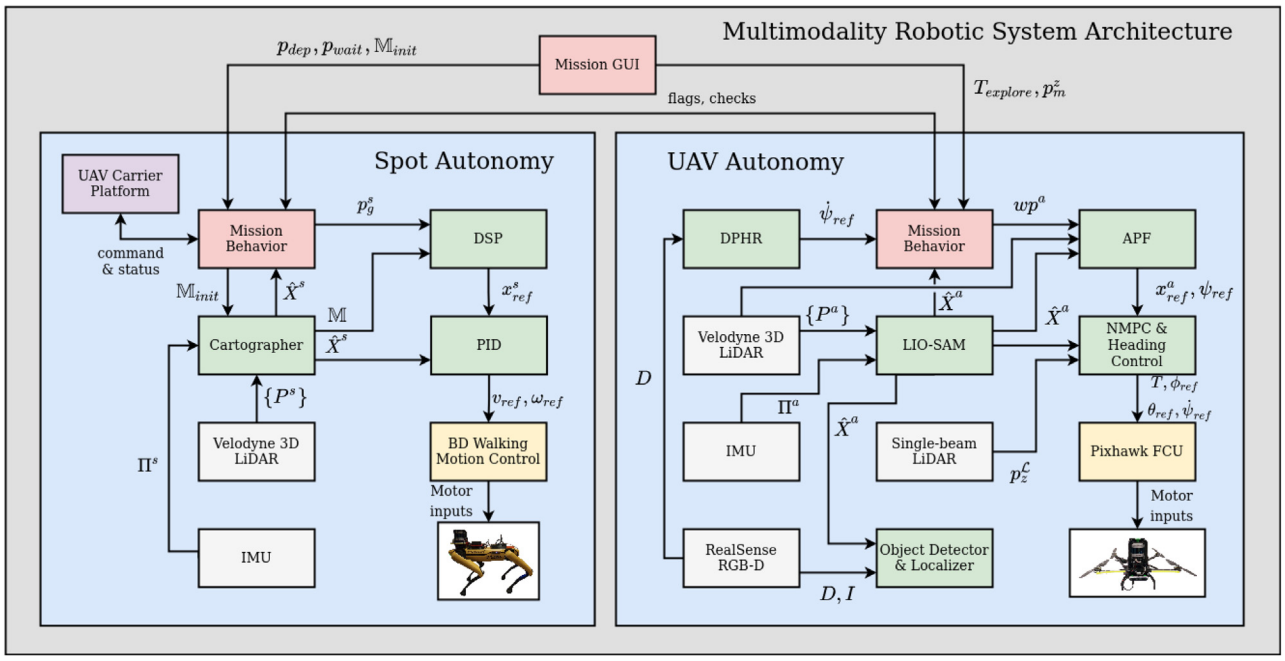

Fig. 5. Complete autonomy architecture used for mission execution. Each component is functionally described in the related Sections 5.2.1 & 5.2.2.

mission z-position reference p_z^m, while utilizing a "carrot-chasing" approach in the body-frame x-axis, such that the next waypoint provided to the potential field is $wp^{a,\mathcal{B}} = [p_x^{\mathcal{B}} + 1, p_y^{\mathcal{B}}, p_z^m]$ commanding the robot towards the deepest point, while letting the potential field handle the maintaining of a safe distance to the walls and any obstacles encountered. Additionally, to return to the deployment point, the UAV follows its previous traveled path back, while still utilizing the APF. Although simplistic, this method of return ensures that the robot follows a return trajectory known to be safe and obstacle free. While the UAV is visiting already known areas, the state-estimation map loop-closure reduces the risk of map/estimation drifts etc.

The visual detection in order to detect, classify, and locate objects is based on the tiny and Intel hardware optimized version [32] of the state of the art CNN object detector Yolo V4 [33]. We trained the network to detect and classify 6 classes defined by the SubT competition using a custom dataset consisting of approximately 700 images for each class. The input size of the images is 416 × 416 and the output of the algorithm is the detected bounding boxes and the class probability.

The other component of the pipeline is the object localizer, which receives the bounding box measurements from the RGB image stream I. The localizer transfers the identified bounding box in the aligned depth image stream D and extracts the relative position of the object compared to the flying platform in the camera frame. Finally the object location $\mathbb{OL}$ is converted to the global world/map frame. The object detection and localization pipeline are depicted in Fig. 6.

5.2.2. Spot autonomy

Spot comes with a local autonomy package, that accepts velocity and angular velocity commands and performs very local avoidance (preventing Spot from walking into an object) based on the out-of-the-box sensor suite. These built-in capabilities of Spot are not sufficient for long and complex autonomous missions or missions in unknown environments. To enable Spot for the autonomous mission, using the sensor suite presented in Section 4.2, the additional software is described in this section. To enable navigation to the deployment point (p_{dep}) a map $\mathbb{M}_{init}$ is needed of the area. The Spot autonomy uses the SLAM package Cartographer [34], due to its capability to map an area and relocalize on that map. Cartographer operates in two steps, the first is an offline map building step and the second step is an online relocalization and mapping algorithm. The fists step uses recorded IMU and LiDAR data (from a previous mission) to build $\mathbb{M}_{init}$ and store for future use. Cartographers second stage loads $\mathbb{M}_{init}$, and with live data from IMU and LiDAR a sub-map (small section of the map) is created, that is matched to $\mathbb{M}_{init}$ and then updates it to a live map $\mathbb{M}$. When Cartographer finds a match between the current sub-map and $\mathbb{M}$ a relocalization is made, and Spots current state X^s in $\mathbb{M}$ is estimated. $\mathbb{M}$ is then procedurally updated from new LiDAR scans.

To navigate from X^s to p_g^s we use a risk-aware gridsearch algorithm, denoted as D_+^* (DSP). DSP extends the D*-lite [35] path planning algorithm by adding a consideration of unknown space, a risk-aware layer, and an update-able/expandable map. The construction of DSP's internal gird map $\mathbb{G}$ is build from $\mathbb{M}$ in such a way that each cell c in $\mathbb{G}$ has a traversal cost ζ corresponding to weather c is free (c_f), occupied (c_o) or unknown (c_u). DSP plans a path $\vec{P}_{X^s \to p_g^s}$ based on $\zeta \in \mathbb{G}$ so that $\sum \forall \zeta \in \vec{P}_{X^s \to p_g^s}$ is as small as possible.

Imperfections in $\mathbb{M}$ can create holes/gaps in $\mathbb{G}$ that may lead to shortcutting and invalid paths, as in Fig. 7(a). With ζ assigned to c so that $\zeta_f < \zeta_u < \zeta_o$, the resulting path $\vec{P}$ is planned in known space only whenever possible and only use unknown space if no other option exist.

A traversal risk is added to the c's next to c_o to introduce a safety marginal to obstacles, leading to safer $\vec{P}$. Without the risk layer, is DSP prone to cut corners and thus potentially collide with the environment. ζ is assigned relative to the proximity to a c_o, resulting in that ζ for a given c will be

$$\zeta_r = \begin{cases} \frac{\zeta_u}{d+1} & \text{if } d < r \\ 0 & \text{else} \end{cases} \tag{2}$$

$$\zeta = \begin{cases} \zeta_f + \zeta_r & \text{if } c \text{ is } c_f \\ \zeta_u + \zeta_r & \text{if } c \text{ is } c_u \end{cases} \tag{3}$$

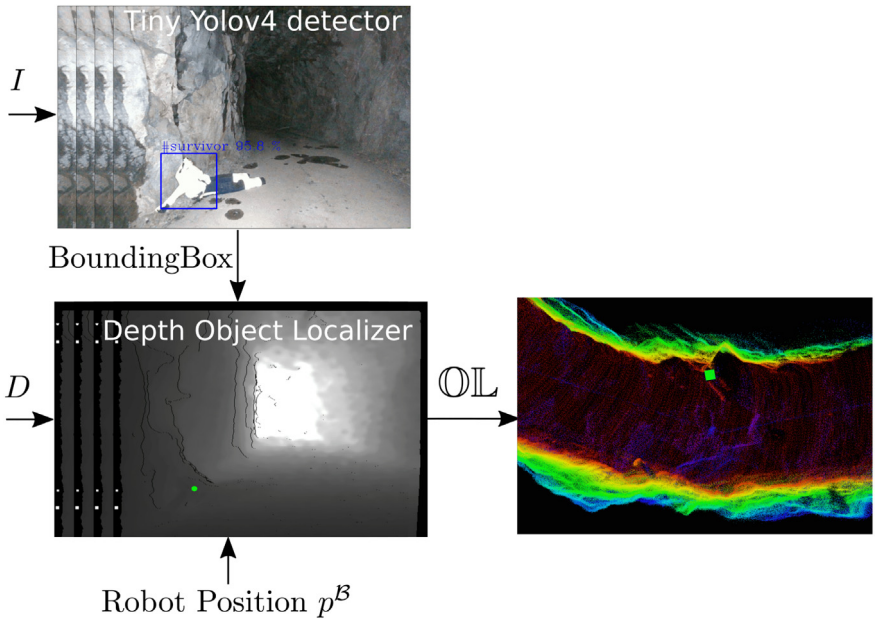

Fig. 6. The object detection and localization pipeline.

where d is the distance in numbers of cells to the closest c_o and r is the max range that is considered as a high-risk area. This creates a gradient risk that is highest next to c_o and decreases with distance as in Fig. 7(b) where cells c with risk-cost ζ_r are shown. Additionally, by tuning the gradient decrease and voxel size to match the robot size the resulting path planner also considers robot-safe paths in addition to avoiding general risky areas.

Spot follows $\bar{P}$ given by DSP with a PID position and heading controller that generates velocity and heading rate commands $u^s = [v_{ref}, \omega_{ref}]$ to Spots internal walking motion controller. Heading references are generated to always face the next waypoint in the path, as forward locomotion is the most efficient for the quadruped robot, while DSP re-calculates paths to compensate for environment changes at around 10 Hz intervals. The full autonomy system on Spot is thoroughly described in [36].

5.3. Mission behavior

In order to execute the mission described in Section 5.1, the robots follow a baseline mission behavior list, where each block is executed in order and considered completed by a condition as for example the mission time $T_m \geq T_{explore}$, or the robot reaching the desired deployment point p_{dep}. The behavior lists for baseline mission execution can be found in Fig. 8.

6. Results

6.1. GUI operations

The combined robotic system is controlled via a mission GUI. A single Operator specifies the desired deployment point of the aerial agent p_{dep} in $\mathbb{M}_{init}$, together with the exploration duration of the aerial mission $T_{explore}$ and the exploration altitude p_z^m. Additionally, the legged robot is tasked to wait at a specified point, p_{wait} until aerial agent return. After the operator launches the mission from the GUI, all aspects are handled completely autonomously and no operator input is required.

6.2. Experiment set-up

The presented submodules are written in C++, Python, and Rust, while we are utilizing ROS [37] for the information flow between submodules and ROS-multimaster [38] for legged-aerial communication utilizing the UAV's local wifi. The experimental evaluation was performed at a field site below Mjölkuddsberget in Luleå, northern Sweden. The site consists of 3–5 meters wide rough-cut tunnel areas currently used for storage, and mimics a real subterranean application site (caves, mining areas, lava tubes) relatively well, see Fig. 9 for schematics and examples of the site. The proposed mission was initialized at the entrance to the site, and the aerial agent deployment point was selected at the main junction that expands in three different directions, (i) right, (ii) forward and (iii) left. Overall, three aerial missions were launched from the junction, one in each direction. We performed one longer mission that explores the right junction direction (seen in Fig. 10), and two shorter missions (one in the forward direction and one in the left direction) where we also added a blockage at the start of the tunnel that disallowed Spot to enter.

Moreover, We placed several artifacts based on the SubT dataset along the tunnels selected for aerial exploration: a hard hat, a survivor, a rope, a drill and a backpack where placed in the right direction experiment, a backpack, a rope and a drill where placed in the forward direction and a survivor artifact was placed in the left direction. A safety pilot and an operator follows the robots during the active mission in case of complete system failure, but do not interact with the them in any way.

6.3. Field evaluation

The maps of the subterranean environments produced during the full mission in the right junction side can be seen in Fig. 10 and in Fig. 11, showing a pointcloud map of the explored environment, as well as detected artifact locations. In Fig. 12 snap shot images of critical points during the mission are displayed such as: the combined system after successfully navigating to the deployment point, the aerial agent initialization and take-off, artifact detection using the onboard camera during COMPRA mission and finally the return to the deployment point of the

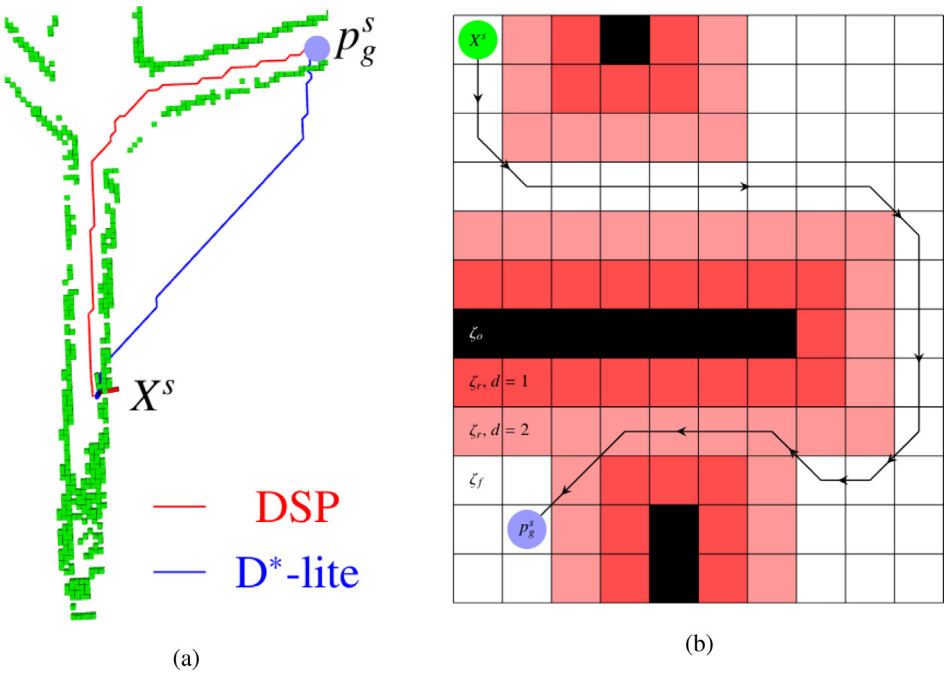

Fig. 7. (a) Paths with and without risk costs. Small gaps in the grid map can lead to incorrect path generation. (b) The DSP concept: the computed path avoids the high-risk areas and only enters them when forced in order to reach the goal.

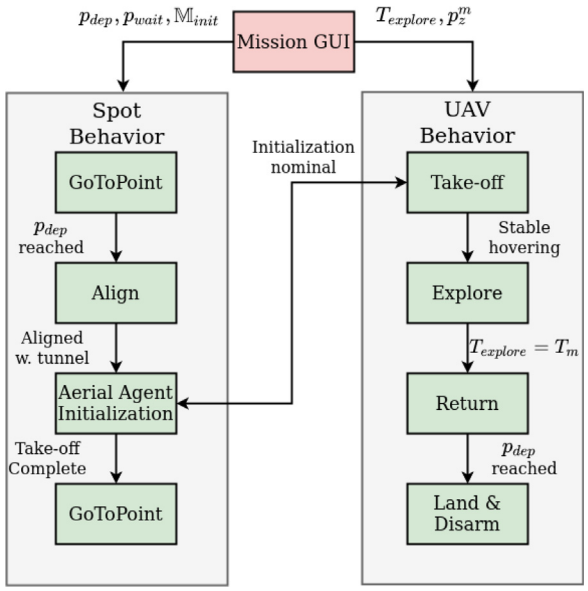

Fig. 8. Behavior lists for specific mission execution for the aerial-legged robot.

aerial agent. Fig. 13 shows the progression of generated DSP paths for the longer full mission for Spot to reach the deployment point.

During the mission, the robots covered approximately 231 m, including the aerial agent's return to the deployment point. Additionally, the two shorter missions were performed in different parts of the same underground tunnel area to showcase the effectiveness to operate and deploy the developed legged-aerial combined system in varying areas (obstacles, inclined, blocked, curving). The resulting pointcloud map overlaid with the localized artifacts, the robot path, and the aerial robot deployment location for the forward direction mission, are depicted in Fig. 14. Fig. 15 presents snap shot images from the experiment including the static obstacles in the tunnel and the detected artifacts from the onboard RGB camera. Similarly, Fig. 16 presents the generated map with overlaid information for the left direction mission and finally, Fig. 17 depicts snap shot images of the blocked passage, an instance of the UAV navigation above the blocked passage, and the detected survivor artifact. This mission showcases the application scenario of where the legged robots traversability is limited and it cannot enter the area. Fig. 18 shows how the explored area is extended by the UAV mission, and the total volumetric gain (or explored volume, using [39]) during that mission for each robot. Only through using the multimodal locomotion could the blocked tunnel be explored and the survivor detected.

For a clear demonstration of the mission capabilities, we strongly recommend the reader to watch the video from the experiment found at https://youtu.be/0p56NkUD_Q8. All considered submodules performed as desired (state estimation, robot re-localization, mapping, aerial agent initialization, navigation, object detection) and the mission was completed as per the mission criteria of detecting the placed artifacts/objects of interest. Fig. 19 shows the minimum range LiDAR measurements throughout the three mission scenarios, and as can be seen both the DSP and APF frameworks are capable of maintaining a safe distance to any walls or encountered obstacles despite the constrained subterranean environment. The smallest measured distance from the environment to the robot was 0.8 m and occurred during the carrying phase of the longer mission. The system has a safety-critical radius of around 0.6 m considering the around 0.4 m size radius of the UAV (with propellers), and the 1.1 m length of Spot. In general, the risk-aware DSP and reactive APF kept the robotic system safe during mission execution.

As there was no ground truth positions of the placed artifacts available, there was no way to verify exactly the state estimation and object localizer in terms of absolute accuracy. Moreover, regarding the artifact localization component, the system has been designed in a conservative way for some artifacts (e.g. helmet), to reject the frequent false positive classifications as a helmet of the few white lamps that were located in the ceiling. More specifically, the object localizer based the outlier rejection on two metrics, the confidence probability of the class, which was set to

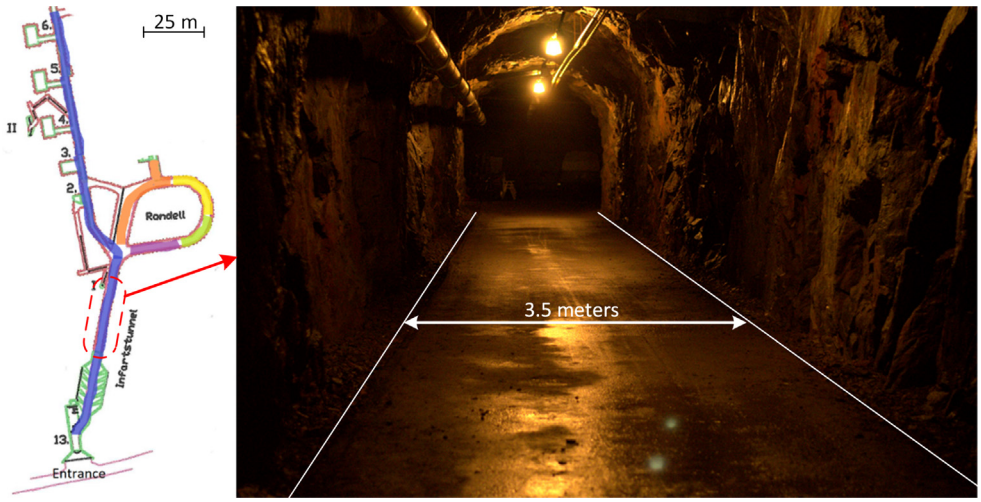

Fig. 9. A schematic of the experiment area (left) and example of the tunnels in which the experimental validation is performed (right).

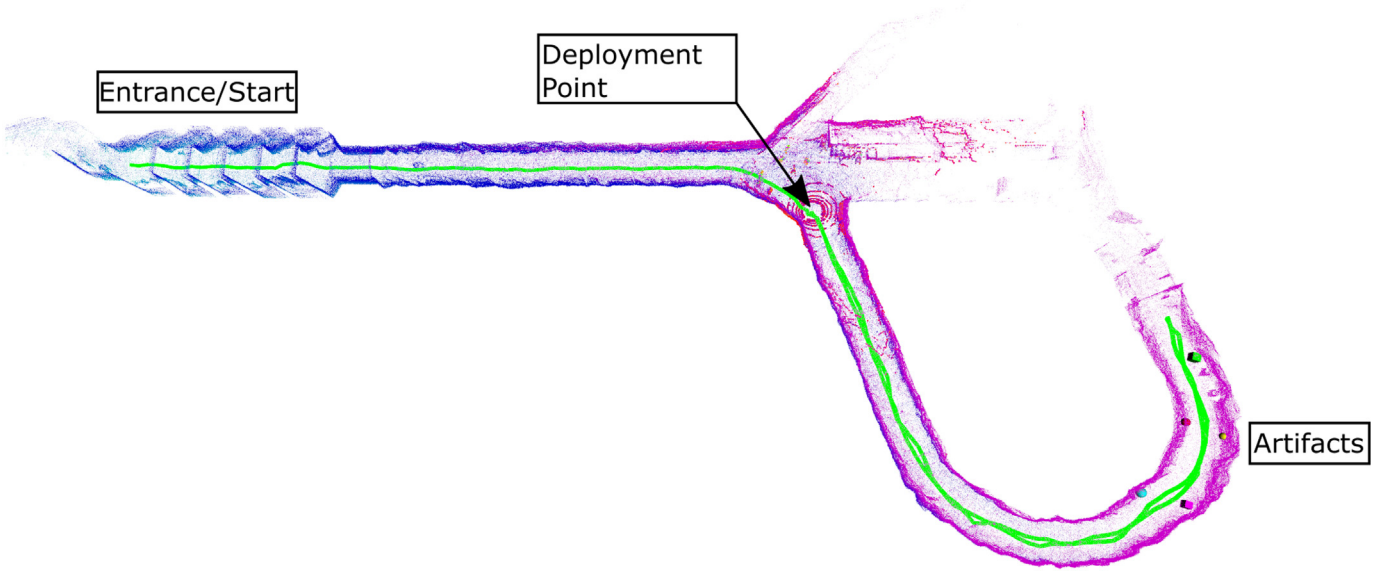

Fig. 10. Final pointcloud map of the explored environment produced during the mission, showing the start of the mission, the aerial agent deployment point and the location of placed artifacts. The green colored line depicts the path traversed by the robot system. (For interpretation of the references to color in this figure legend, the reader is referred to the web version of this article.)

75% for all field trials and the euclidean distance to the artifact $d^{\mathcal{B}}_{artifact} \in [0.2\text{ m}, 6\text{ m}]$, since it was observed from the field trials that the object detector success rate was higher for objects that were closer to the camera. The object detector is also challenged by the fast motion of the aerial platform, the induced motion blur and the short amount of time that an object might be inside the camera's Field of View, which causes in some cases fewer object detections.

In general: utilizing the presented legged-aerial quick deployment framework, the mission was easily repeatable without inconsistencies in mission behavior and without any sub-module failures such as the robots getting stuck, environment interactions, or large state estimation drifts or jumps.

7. Future work

While the proposed autonomy stack allows the robots to perform a full autonomous mission, its range of applications is relatively limited and future research should focus on further, and more fluid, integration of autonomous collaboration between the legged-aerial system and achieving a more unified system. This would include frontier analysis (for exploration) based on the modality of the robot and generating traversability maps that directly considers the dynamics of the robots, resulting in a more complete architecture that can on its own detect when and where the aerial agent should be launched. Adding exploration behavior on Spot would also allow the two robots to separately explore areas simultaneously. Additionally, equipping the legged-aerial system with multiple smaller but lower-autonomy UAVs could greatly increase coverage. Another clear addition is the development of a landing behavior that guides the aerial agent to land back on the UAV carrier platform to complete the aerial mission. This proved to be a difficult task to execute consistently without external localization and sensing, and in the low-light conditions of the SubT area, as the accuracy required is very high. This is something we are currently working on.

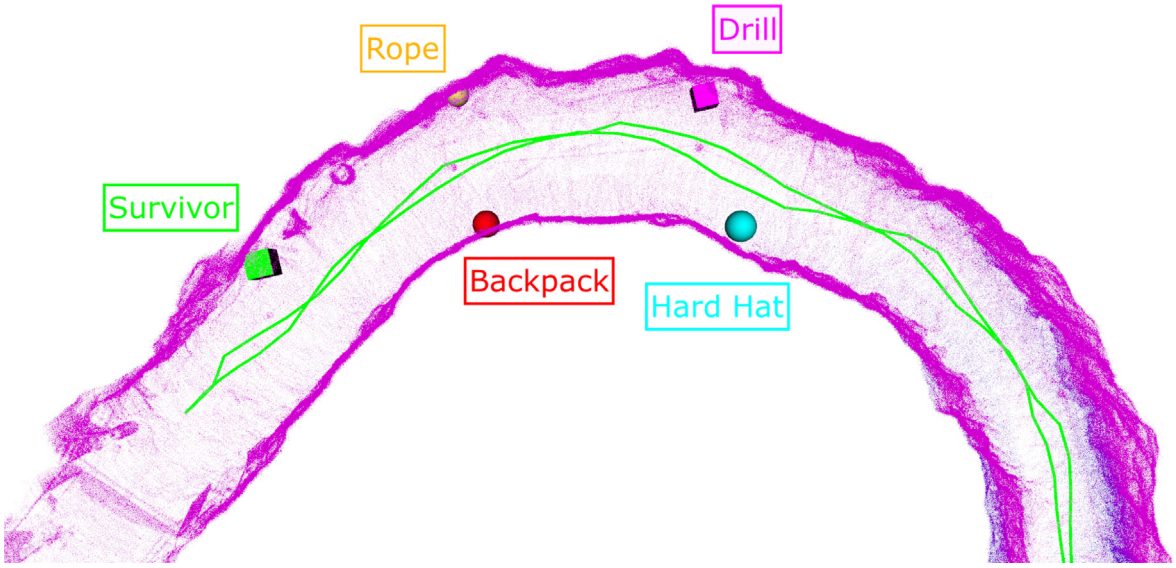

Fig. 11. Detected artifacts and exploration path of the aerial agent.

Fig. 12. Snap shots from the full mission. (a) Multimodality system approaching deployment point, (b) deployment point reached, (c) aerial agent take-off, (d) hard hat detection from onboard camera during COMPRA mission, (e) survivor detection, (f) aerial agent return to deployment point.

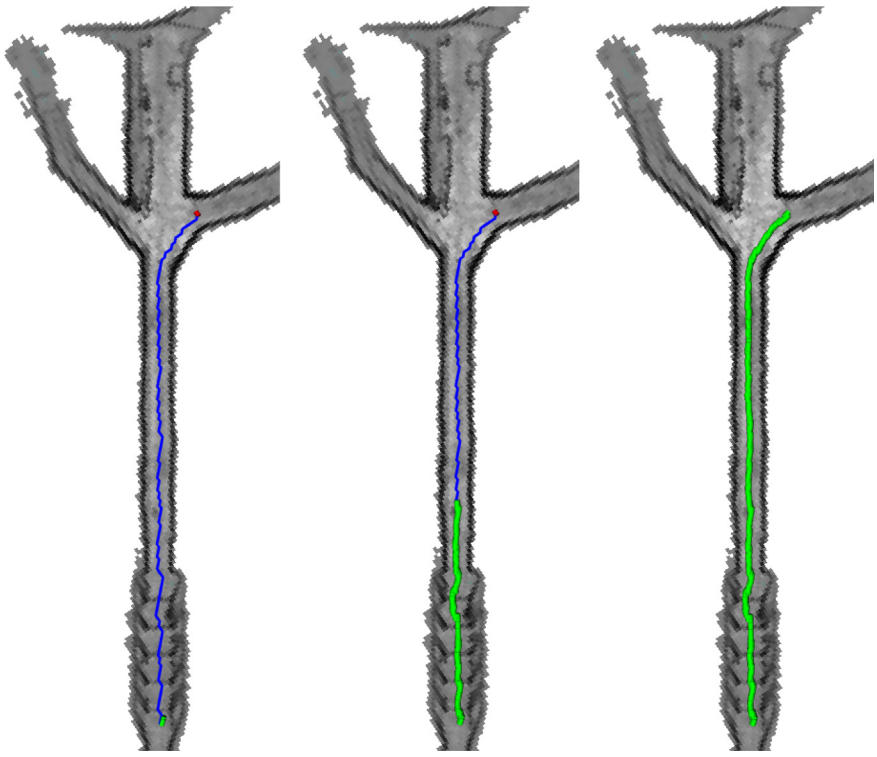

Fig. 13. DSP paths (blue line) to deployment point (red dot) and combined system traversed path (green line). (For interpretation of the references to color in this figure legend, the reader is referred to the web version of this article.)

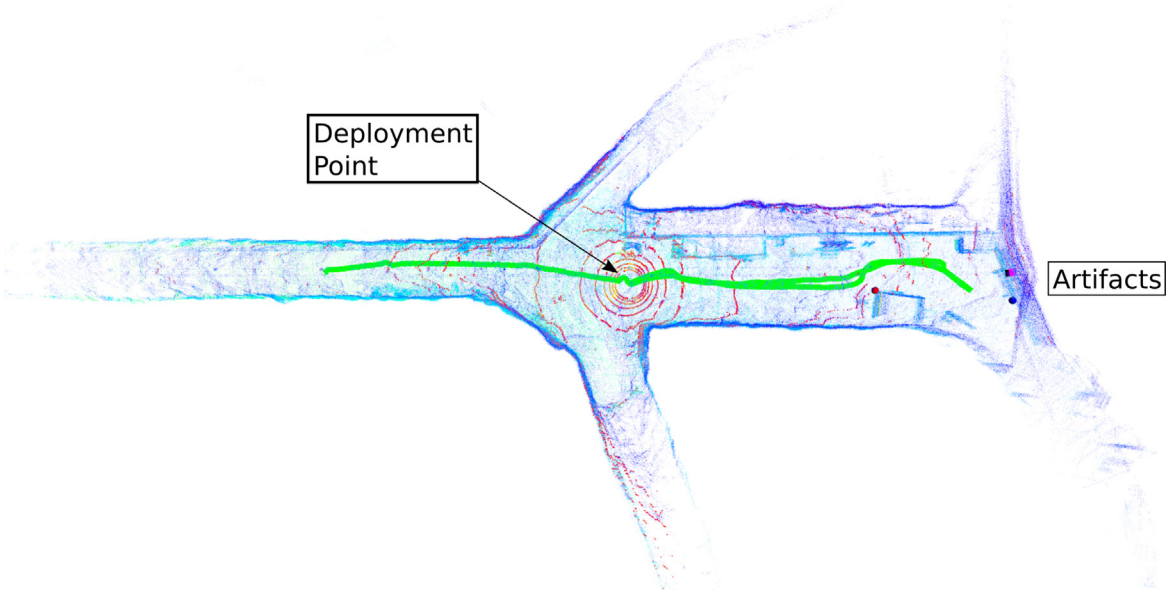

Fig. 14. Resulting sparse pointcloud, detected artifacts and exploration path of the aerial agent during the forward direction experiment.

8. Conclusions

This article has presented a legged-aerial combined robotic system capable of executing search-and-rescue missions in subterranean environments. We have demonstrated a hardware–software integration and architecture, and a mission design that showcases the use of multimodality locomotion for completely autonomous mission execution in GPS- and communication denied environments. The system successfully performed the mission of detecting and localizing the objects of interest placed in the subterranean tunnel areas, while navigation and state estimation modules performed as desired, keeping the robots safe during the mission. Since the combination of a legged-aerial robotic system for subterranean surveying is novel there are multiple directions for future work, especially in the area of robot unification.

Fig. 15. Snap shot of the forward direction mission. (a) Static obstacles along the course, (b) backpack artifact detection, (c) drill artifact detection, (d) rope artifact detection.

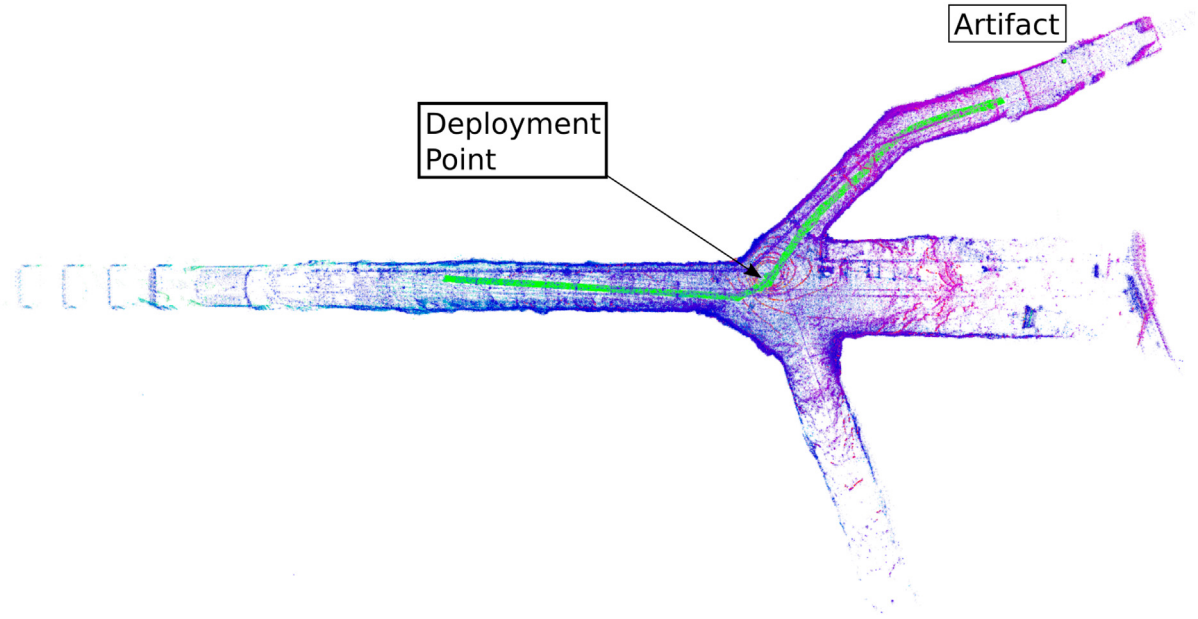

Fig. 16. Resulting pointcloud map, detected artifacts, and exploration path of the aerial agent during the left direction experiment.

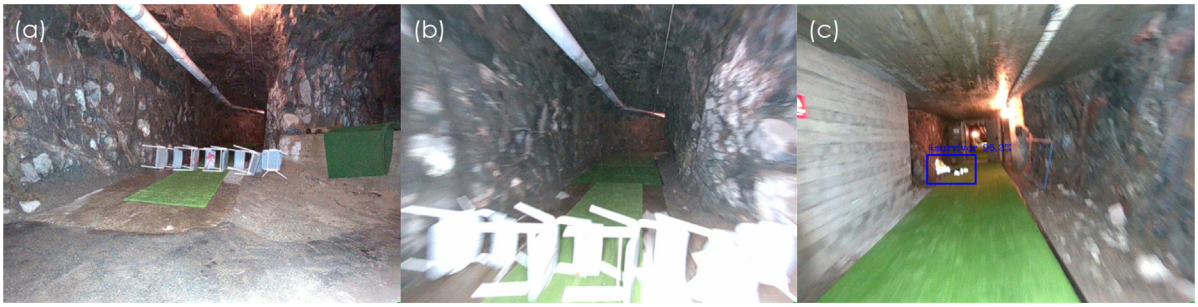

Fig. 17. Snap shot of the left direction mission. (a) Blocked passage for the legged robot, (b) UAV navigating above the blocked passage, (c) survivor artifact detection.

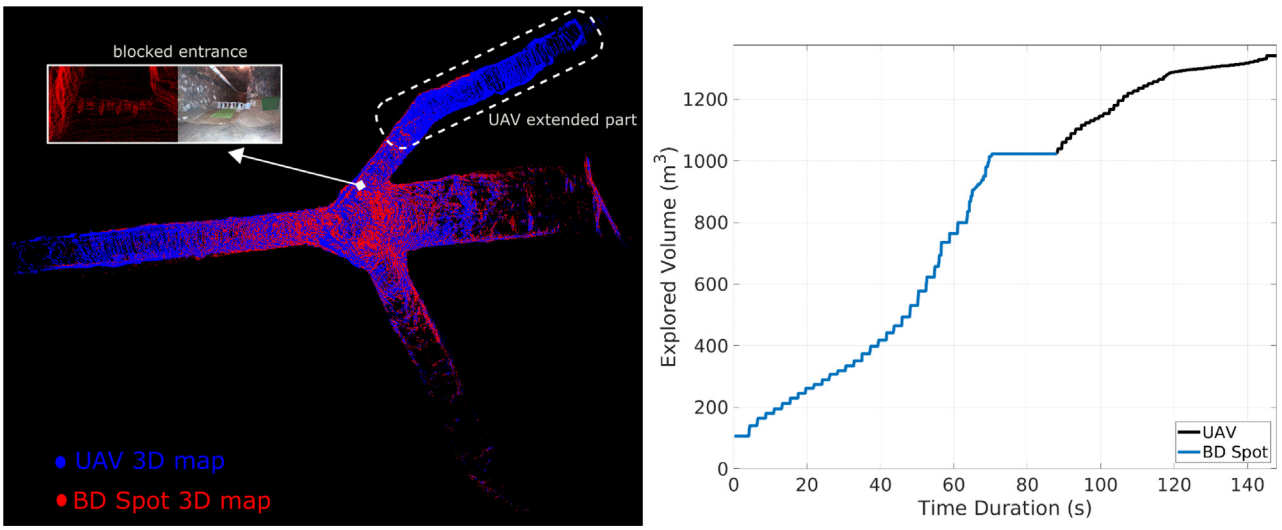

Fig. 18. Overlaid pointcloud maps created by each robot, showing how the map is extended by the aerial agent (left), and the total explored volume from each robot (right), where the aerial agent can continue the mission despite the blockage.

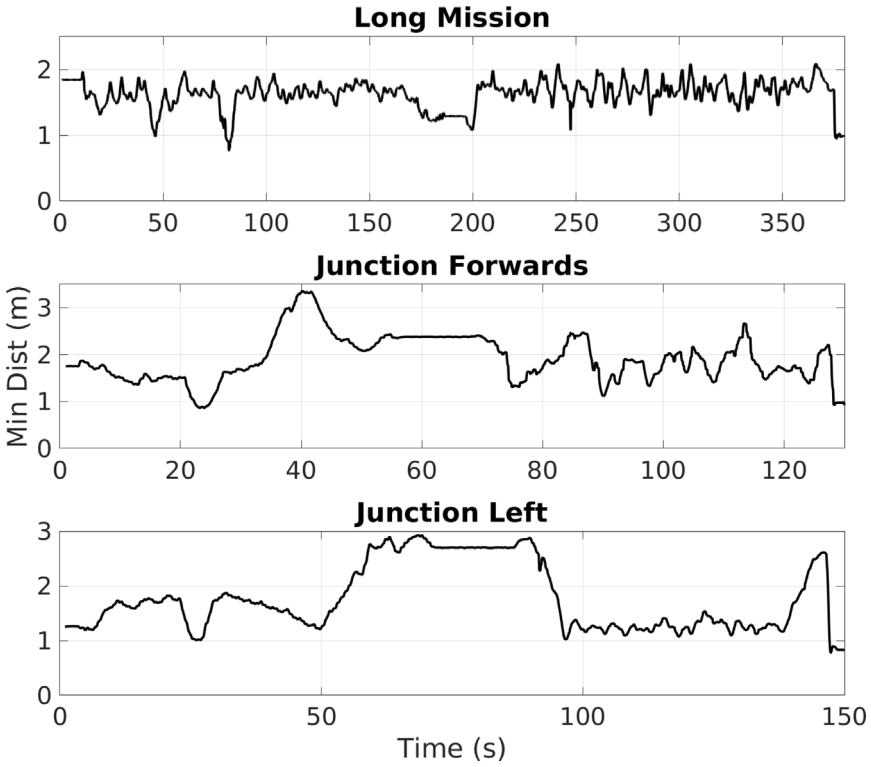

Fig. 19. Minimum safety distances, as the minimum range LiDAR measurement. A 5-point median filter was applied to filter out measurements that hit dust particles.

Declaration of competing interest

The authors declare that they have no known competing financial interests or personal relationships that could have appeared to influence the work reported in this paper.

Acknowledgments

This work has been partially funded in part by the European Unions Horizon 2020 Research and Innovation Programme under the Grant Agreements No. 869379 illuMINEation, No. 101003591 NEXGEN-SIMS and in part by the Interreg Nord Programme ROBOSOL NYPS 20202891.

References

[1] DARPA, Subterranean challenge (SubT). URL https://www.subtchallenge.com/.

[2] M. Dharmadhikari, H. Nguyen, F. Mascarich, N. Khedekar, K. Alexis, Autonomous cave exploration using aerial robots, in: 2021 International Conference on Unmanned Aircraft Systems (ICUAS), IEEE, 2021, pp. 942–949.

[3] P. Petráček, V. Krátkỳ, M. Petrlík, T. Báča, R. Kratochvíl, M. Saska, Large-scale exploration of cave environments by unmanned aerial vehicles, IEEE Robot. Autom. Lett. 6 (4) (2021) 7596–7603.

[4] C. Kanellakis, S.S. Mansouri, G. Georgoulas, G. Nikolakopoulos, Towards autonomous surveying of underground mine using mavs, in: International Conference on Robotics in Alpe-Adria Danube Region, Springer, 2018 pp. 173–180.

[5] S.S. Mansouri, C. Kanellakis, D. Kominiak, G. Nikolakopoulos, Deploying MAVs for autonomous navigation in dark underground mine environments, Robot. Auton. Syst. 126 (2020) 103472.
[6] M. Sarkar, X. Yan, B.A. Erol, I. Raptis, A. Homaifar, A novel search and survey technique for unmanned aerial systems in detecting and estimating the area for wildfires, Robot. Auton. Syst. 145 (2021) 103848, http://dx.doi.org/10.1016/j.robot.2021.103848, URL https://www.sciencedirect.com/science/article/pii/S0921889021001330.
[7] J. Blank, B. Morrell, A. Bouman, T. Touma, M. Ginting, C. Patterson, A. Aghamohammadi, Autonomous mapping and characterization of terrestrial lava caves using quadruped robots: Preparing for a mission to a planetary cave, LPI Contrib. 2595 (2021) 8122.
[8] T.N. Titus, J.J. Wynne, M.J. Malaska, A.-a. Agha-Mohammadi, P.B. Buhler, E.C. Alexander, J.W. Ashley, A. Azua-Bustos, P.J. Boston, D.L. Buczkowski, et al., A roadmap for planetary caves science and exploration, Nat. Astron. 5 (6) (2021) 524–525.
[9] T. Dang, M. Tranzatto, S. Khattak, F. Mascarich, K. Alexis, M. Hutter, Graph-based subterranean exploration path planning using aerial and legged robots, J. Field Robotics 37 (8) (2020) 1363–1388.
[10] T. Dang, F. Mascarich, S. Khattak, C. Papachristos, K. Alexis, Graph-based path planning for autonomous robotic exploration in subterranean environments, in: 2019 IEEE/RSJ International Conference on Intelligent Robots and Systems (IROS), IEEE, 2019, pp. 3105–3112.
[11] A. Agha, K. Otsu, B. Morrell, D.D. Fan, R. Thakker, A. Santamaria-Navarro, S.-K. Kim, A. Bouman, X. Lei, J. Edlund, et al., Nebula: Quest for robotic autonomy in challenging environments; team costar at the darpa subterranean challenge, 2021, arXiv preprint arXiv:2103.11470.
[12] T. Rouček, M. Pecka, P. Čížek, T. Petříček, J. Bayer, V. Šalanskỳ, D. Heřt, M. Petrlík, T. Báča, V. Spurnỳ, et al., Darpa subterranean challenge: Multi-robotic exploration of underground environments, in: International Conference on Modelling and Simulation for Autonomous Systesm, Springer, Cham, 2019, pp. 274–290.
[13] Z.-X. Zhang, Rock mechanics related to mining engineering, in: ISRM 3rd Nordic Rock Mechanics Symposium-NRMS 2017, OnePetro, 2017.
[14] P. Rea, E. Ottaviano, Design and development of an inspection robotic system for indoor applications, Robot. Comput.-Integr. Manuf. 49 (2018) 143–151.
[15] A. Papadimitriou, G. Andrikopoulos, G. Nikolakopoulos, Development and control of a differential wall climbing robot based on vortex adhesion, in: 2019 18th European Control Conference (ECC), IEEE, 2019, pp. 1610–1615.
[16] O. Gerasin, O. Kozlov, G. Kondratenko, J. Rudolph, Y. Kondratenko, Neural controller for mobile multipurpose caterpillar robot, in: 2019 10th IEEE International Conference on Intelligent Data Acquisition and Advanced Computing Systems: Technology and Applications (IDAACS), Vol. 1, IEEE, 2019, pp. 222–227.
[17] Y. Kondratenko, J. Rudolph, O. Kozlov, Y. Zaporozhets, O. Gerasin, Neuro-fuzzy observers of clamping force for magnetically operated movers of mobile robots, Tech. Electrodyn. 5 (2017) 53–61.
[18] Y. Kondratenko, O. Gerasin, O. Kozlov, A. Topalov, B. Kilimanov, Inspection mobile robot's control system with remote IoT-based data transmission, J. Mob. Multimedia (2021) 499–526.
[19] A. Kalantari, T. Touma, L. Kim, R. Jitosho, K. Strickland, B.T. Lopez, A.-A. Agha-Mohammadi, Drivocopter: A concept Hybrid Aerial/Ground vehicle for long-endurance mobility, in: 2020 IEEE Aerospace Conference, IEEE, 2020, pp. 1–10.
[20] G. Nikolakopoulos, A. Agha, Pushing the limits of autonomy for enabling the next generation of space robotics exploration missions, Computer 54 (11) (2021) 100–103.
[21] S.-K. Kim, A. Bouman, G. Salhotra, D.D. Fan, K. Otsu, J. Burdick, A.-a. Agha-mohammadi, PLGRIM: Hierarchical value learning for large-scale exploration in unknown environments, in: Proceedings of the International Conference on Automated Planning and Scheduling, Vol. 31, 2021, pp. 652–662.
[22] M. Palieri, B. Morrell, A. Thakur, K. Ebadi, J. Nash, A. Chatterjee, C. Kanellakis, L. Carlone, C. Guaragnella, A.-a. Agha-Mohammadi, Locus: A multi-sensor lidar-centric solution for high-precision odometry and 3d mapping in real-time, IEEE Robot. Autom. Lett. 6 (2) (2020) 421–428.
[23] TEAM COSTAR, NeBula autonomy. URL https://costar.jpl.nasa.gov/.
[24] B. Lindqvist, C. Kanellakis, S.S. Mansouri, A. akbar Agha-mohammadi, G. Nikolakopoulos, C?ompra: A COMPact Reactive Autonomy framework for subterranean MAV based search-and-rescue operations, 2021, arXiv:2108.13105.
[25] T. Shan, B. Englot, D. Meyers, W. Wang, C. Ratti, D. Rus, LIO-SAM: Tightly-coupled lidar inertial odometry via smoothing and mapping, in: IEEE/RSJ International Conference on Intelligent Robots and Systems (IROS), 2020.
[26] E. Small, P. Sopasakis, E. Fresk, P. Patrinos, G. Nikolakopoulos, Aerial navigation in obstructed environments with embedded nonlinear model predictive control, in: 2019 18th European Control Conference (ECC), IEEE, 2019, pp. 3556–3563.
[27] B. Lindqvist, S.S. Mansouri, A.-a. Agha-mohammadi, G. Nikolakopoulos, Nonlinear MPC for collision avoidance and control of UAVs with dynamic obstacles, IEEE Robot. Autom. Lett. 5 (4) (2020) 6001–6008.
[28] L. Meier, P. Tanskanen, F. Fraundorfer, M. Pollefeys, Pixhawk: A system for autonomous flight using onboard computer vision, in: 2011 IEEE International Conference on Robotics and Automation, IEEE, 2011 pp. 2992–2997.
[29] L. Meier, D. Honegger, M. Pollefeys, PX4: A node-based multithreaded open source robotics framework for deeply embedded platforms, in: 2015 IEEE International Conference on Robotics and Automation (ICRA), IEEE, 2015, pp. 6235–6240.
[30] C.W. Warren, Global path planning using artificial potential fields, in: 1989 IEEE International Conference on Robotics and Automation, IEEE Computer Society, 1989, pp. 316–317.
[31] P. Soille, Morphological Image Analysis: Principles and Applications, second ed., Springer-Verlag, Berlin, Heidelberg, 2003.
[32] Intel, OpenVINO™ Toolkit. URL https://docs.openvinotoolkit.org/latest/index.html.
[33] A. Bochkovskiy, C.-Y. Wang, H.-Y.M. Liao, Yolov4: Optimal speed and accuracy of object detection, 2020, arXiv preprint arXiv:2004.10934.
[34] W. Hess, D. Kohler, H. Rapp, D. Andor, Real-time loop closure in 2D LIDAR SLAM, in: 2016 IEEE International Conference on Robotics and Automation (ICRA), IEEE, 2016, pp. 1271–1278.
[35] M. Sheckells, DSL GridSearch: D*-lite on a uniformly spaced 3D or 2D grid, 2018, Accessed: February 2021. URL https://github.com/jhu-asco/dsl_gridsearch.
[36] A. Koval, S. Karlsson, G. Nikolakopoulos, Experimental evaluation of autonomous map-based spot navigation in confined environments, Biomim. Intell. Robot. (2022) 100035.
[37] M. Quigley, K. Conley, B. Gerkey, J. Faust, T. Foote, J. Leibs, R. Wheeler, A.Y. Ng, et al., ROS: an open-source robot operating system, in: ICRA Workshop on Open Source Software, Vol. 3, Kobe, Japan, 2009, p. 5.
[38] A. Tiderko, F. Hoeller, T. Röhling, The ROS multimaster extension for simplified deployment of multi-robot systems, in: Robot Operating System (ROS), Springer, 2016, pp. 629–650.
[39] C. Cao, H. Zhu, F. Yang, Y. Xia, H. Choset, J. Oh, J. Zhang, Autonomous exploration development environment and the planning algorithms, 2021, arXiv preprint arXiv:2110.14573.

Björn Lindqvist is currently pursuing his Ph.D. at the Robotics and AI Team at the Department of Computer Science, Electrical and Space Engineering, Luleå University of Technology, Sweden, working in the field of aerial robotics. He received his Master's Degree in Space Engineering with a specialization Aerospace Engineering from Luleå University of Technology, Sweden, in 2019. Björn's research has so far been focused on collision avoidance and path planning for single and multi-agent Unmanned Aerial Vehicle systems, as well as field applications of such technologies. He has worked as part of the JPL-NASA led Team CoSTAR in the DARPA Sub-T Challenge on subterranean UAV exploration applications, specifically in the search-and-rescue context.

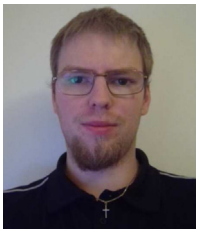

Samuel Karlsson is currently pursuing his Phd at the Robotics and AI Team at the Department of Computer Science, Electrical and Space Engineering, Luleå University of Technology, Sweden, working in the field of areal and ground robotic. He received his master's degree in Computer science and engineering with specialization in industrial computer systems from Luleå University of Technology, Sweden, in 2020. Samuel's research has so far been focused on risk aware path planning for safe navigation of aerial and ground robots. He has worked as part of the JPL-NASA led Team CoSTAR in the DARPA Sub-T Challenge on subterranean UAV exploration applications, specifically in the search-and-rescue context.

Anton Koval is a post-doctoral researcher at the Department of Computer Science, Electrical and Space Engineering at the Luleå University of Technology, Sweden. He received his Ph.D. from National Technical University of Ukraine "Kyiv Polytechnic Institute", Ukraine in 2012. He has been involved in several European and Ukrainian National projects on micro aerial vehicles and environmental monitoring. In 2018 he received the Swedish Institute Visby scholarship for senior scientists for 6 months at Luleå University of Technology, Sweden. His current research interests are mainly focused on control, exploration and path planning with multiple agents.

Ilias Tevetzidis is a research engineer working alongside the robotics & AI team at Luleå University of Technology. He received his bachelor's degree in Automotive engineering from Luleå University of Technology in 2020 and he specializes in electronics and software–hardware integration. He is currently a part of, and working with, many national and international projects in robotics & AI as well as teaching at Luleå University of Technology.

Jakub Haluška received a Master's degree in Mechanical Engineering from the Technical University of Liberec, Czech Republic, in 2019. He is currently a Research Engineer within the Control Engineering Group, Department of Computer Science, Electrical and Space Engineering, Luleå University of Technology (LTU). His focus is on the design and construction of robust and field-applicable robots as well as 3D printing technologies.

Christoforos Kanellak is currently works as an Associate Senior Lecturer at Luleå University of Technology. Christoforos received his Ph.D degree within the Control Engineering Group, Department of Computer Science, Electrical and Space Engineering, Luleå University of Technology (LTU), Luleå, Sweden. He received his Diploma from the Electrical & Computer Engineering Department of the University of Patras (UPAT), Greece in 2015. He currently works in the field of perception for robotics, focusing on the combination of control and vision to enable robots perceive and interact with the environment.

Ali-akbar Agha-mohammadi is a robotics research technologist with NASA's Jet Propulsion Laboratory (JPL), Caltech. Previously, he was an autonomy research engineer with Qualcomm Research and a postdoctoral researcher with the Laboratory for Information and Decision Systems at Massachusetts Institute of Technology. He received his Ph.D. from Texas A&M University, and his research interests include robotic autonomy, mobility and perception, stochastic control systems and filtering theory. Agha manages several projects at JPL on autonomy, control and perception for robotic systems (rovers and aerial vehicles). He was selected as a NASA NIAC Fellow in 2018.

George Nikolakopoulos works as the Chair Professor in Robotics and Artificial Intelligence, at the Department of Computer Science, Electrical and Space Engineering, Luleå University of Technology (LTU), Sweden. He was also affiliated with the NASA Jet Propulsion Laboratory for conducting collaborative research on Aerial Planetary Exploration and participated in the DARPA Grand challenge on Sub-T exploration with the CoSTAR team of JPL-NASA. He is a Director of euRobotics, and is a member of the Scientific Council of ARTEMIS and the IFAC TC on Robotics. He established the Digital Innovation Hub on Applied AI at LTU and also represents Sweden in the Technical Expert Group on Robotics and AI in the project MIRAI 2.0 promoting collaboration between Sweden and Japan. His main research interests are in the areas of: Field Robotics, Space Autonomy, UAVs, Automatic Control Applications, Networked Embedded Controlled Systems, Wireless Sensor and Actuator Networks, Cyber Physical Systems, and Adaptive Control.